SCIENTIFIC REPORTS

OPEN

Topological insulator with negative spin-orbit coupling and transition between Weyl and Dirac semimetals in InGaN-based quantum wells

S. P. Łepkowski [1] & W. Bardyszewski[2]

We study the influence of negative spin-orbit coupling on the topological phase transition and properties of the topological insulator state in InGaN-based quantum wells grown along *c* axis of the wurtzite lattice. The realistic eight-band *k·p* method with relativistic and nonrelativistic linear-*k* terms is employed. Our calculations show that the negative spin-orbit coupling in InN is not an obstacle to obtain the topological insulator phase in InN/InGaN and InGaN/GaN quantum wells. The bulk energy gap in the topological insulator state can reach 2 meV, which allows experimental verification of the edge state transport in these materials. The topological phase transition occurs due to the band inversion between the highest light hole subband and the lowest conduction subband, and almost always is mediated by the two-dimensional Weyl semimetal, arising from an anticrossing of these subbands at zero in-plane wave vector. However, for certain InGaN/GaN quantum wells, we find that the magnitude of this anticrossing vanishes, leading to the appearance of the Dirac semimetal. The novel transition between the Weyl and Dirac semimetals originates from vanishing of the average in-plane spin-orbit interaction parameter, which decouples the conduction subband from the light hole subband at zero in-plane wave vector.

The discovery of the time–reversal topological insulators (TIs) in two and three dimensions has greatly inspired the study of topological properties of the electronic band structure of crystalline materials[1]. The TIs are characterized by an energy gap in the bulk electronic band structure and metallic states on the boundaries. Closing of the band gap by the surface or edge states is caused by the nontrivial topology of the bulk states, originating from an inversion in the order in the valence and conduction bands at time reversal invariant wave vectors in the Brillouin zone (BZ)[1]. This band inversion changes the Z_2 topological invariant leading to the topological phase transition (TPT) from the normal insulator (NI) to the TI state[1]. The nature of the TPT depends on the dimensionality and crystal symmetry of the systems[2–11]. In three-dimensional (3D) crystals without inversion symmetry, the TPT is mediated either by a stable Weyl semimetal (WSM) phase with separated Weyl points or a nodal-line semimetal having a line nodes along which the band gap closes[2,3]. When the system has inversion symmetry, a direct transition between the NI and TI phases occurs through a critical point corresponding to a Dirac semimetal (DSM)[2,3]. The DSMs arising in the TPT are generally not robust against small perturbations and in certain cases they can be stabilized by the crystal symmetry. The symmetry protected Dirac states occur at high-symmetry points on the surface of the BZ in crystals with the nonsymmorphic space group symmetries or at generic points on a n-fold symmetry axis inside the BZ, where the mixing between the inverted bands is forbidden by the different rotational symmetries[4,5]. Recently, it has also been found that in the 3D systems, it is possible to induce the TPT without closing of the band gap, which can happen due to a jump between two band gap minima in the free energy corresponding to the NI and TI states[6].

[1]Institute of High Pressure Physics, "Unipress", Polish Academy of Sciences, ul. Sokołowska 29/37, 01-142, Warszawa, Poland. [2]Faculty of Physics, University of Warsaw, ul. Pasteura 5, 02-093, Warszawa, Poland. Correspondence and requests for materials should be addressed to S.P.Ł. (email: slawek@unipress.waw.pl)

In two-dimensional (2D) nanostructures, the TPT is always accompanied by the closing of the bulk band gap, and the character of the intermediate gapless states depends on the full crystal symmetry of the multilayer structures[6–11]. In conventional 2D topological materials, such as zinc-blende HgTe/CdTe and InAs/GaSb/AlSb quantum wells (QWs), the band inversion occurs in the center of the BZ, and the TPT is mediated either by the DSM or by the WSM, depending whether the conduction band (CB) and the valence band (VB) states cross or anticross at zero in-plane wave vector ($k_\perp = 0$), respectively[8–10]. When the QW structure is oriented along [001] crystallographic direction, both the CB and heavy hole (HH) states transform according to the same spinor representations, and thus, they anticross at $k_\perp = 0$, generating the WSM at the boundary between the NI and TI states[8–10]. Recently, it has been shown that the WSM in these nanostructures is a stable phase due to the combination of time-reversal symmetry with twofold rotation symmetry[11]. On the other hand, in HgTe/CdTe QWs grown along [111] crystallographic direction, the CB and HH states transform according to different irreducible representations[8], leading to the subband crossing at $k_\perp = 0$. Therefore, in these QWs, one can expect an appearance of an unstable DSM, which is induced by the crystal symmetry of the nanostructure, but is not protected against perturbations. It differs from the symmetry protected 2D DSMs, in which the Dirac points appear at the boundary of the BZ, in the systems with nonsymmorphic symmetries[12].

In this work, we demonstrate that the TPT in a QW system built from materials with different signs of the effective spin-orbit coupling (SOC) can be mediated by the WSM and the DSM, which opens a unique possibility to induce the transition between these two gapless states without changing the system symmetry or the reordering of the valence subbands. In such a case, the DSM can appear during the TPT, though the CB and VB states at $k_\perp = 0$ transform according to the same irreducible representations. We study InGaN-based QWs, for which the TI state can be reached thanks to the large built-in electric field originating from the piezoelectric effect and the spontaneous polarization[13–16]. The idea of using the external or built-in electric field to transform the nontopological QW system to topological one was initially proposed for HgCdTe/CdTe and InAs/GaSb/AlSb QWs and recently, it has been extended to InGaN/GaN, Ge/GaAs and InSb/CdTe quantum heterostructures[13–20]. Although wurtzite group-III nitrides are technologically important semiconductors, the issue of the SOC in these materials is still under scientific debate. For many years, the sequence of the valence bands in wurtzite GaN and InN was believed to be the same, namely the HH band with the Γ_9 symmetry is above two Γ_7 bands termed as the light hole (LH) and the crystal field split-off bands. This ordering of the valence bands corresponds to the positive SOC, determined by the positive values of two SOC parameters $\Delta_{so}^{\parallel}$ and $\Delta_{so}^{\perp}$, which are referred to as the SOC constants along the c axis of the wurtzite lattice and in the plane perpendicular to the c axis, respectively. The reported values of $\Delta_{so}^{\parallel}$ and $\Delta_{so}^{\perp}$ in InN and GaN, obtained from *ab-initio* band structure calculations and experiments, were in the range from 1 to 25 meV[21–23]. The positive SOC in GaN and InN was taken into account so far in the study of the TPT in InN/GaN and InGaN/GaN QWs[13–15]. In such a case, the TPT is mediated by the DSM arising from the crossing of the HH and CB subbands at $k_\perp = 0$[14]. The 2D bulk energy gap (E_{2Dg}) in the TI state was found to reach about 5 meV[14,15] and 10 meV[13]. These significant values of E_{2Dg} allow experimental verification of the edge state transport in InN/GaN and InGaN/GaN QWs and also motivate design of new topological devices based on these structures[24,25]. However, recent state of the art *ab-initio* calculations, performed using the quasiparticle self-consistent GW method, have shown that the effective SOC in InN is negative with $\Delta_{so}^{\parallel}$ and $\Delta_{so}^{\perp}$ equal to -9.5 and -5.9 meV, respectively[26]. Consequently, the ordering of the valence bands in InN is anomalous with the LH Γ_7 band above the HH Γ_9 band[26]. The negative SOC was also found in zinc-blende HgS and in wurtzite ZnO and TlN[27–29]. TlN has additionally inversion of the CB and VB states in the center of the BZ, which makes it a unique 3D TI with the negative SOC[29].

Here, we investigate the influence of the negative SOC on the TPT and the properties of the TI state in InGaN-based QWs grown along the c axis (see Fig. 1). We employ the realistic eight-band $k \cdot p$ method, which includes relativistic and nonrelativistic linear in k terms (see the Methods section). Our calculations show that the negative SOC in InN is not an obstacle to induce the TI phase in InN/InGaN and InGaN/GaN QWs. The E_{2Dg} in the TI state can reach 2 meV, which enables detection of edge state transport in reasonable experimental conditions. The TPT occurs due to the band inversion between the highest LH subband and the lowest CB subband, and almost always is mediated by the WSM due to the anticrossing of the CB and LH levels at $k_\perp = 0$. However, for certain InGaN/GaN QWs, we find that this level anticrossing vanishes, leading to the appearance of the DSM at the boundary between the NI and TI phases. Thus, we reveal a novel transition between the WSM and the DSM and show that it originates from vanishing of the average $\Delta_{so}^{\perp}$ parameter over a QW structure.

Results and Discussion

We consider first InN/GaN multi-QWs with the QW width, $L_{qw} = 1.25$ nm, corresponding to 4 monolayers of InN, for which the band structure can be inverted by the built-in electric field[13]. A disadvantage of these nanostructures is significant internal strain, which arises from large lattice misfit between GaN and InN, and causes difficulties in pseudomorphic growth of sufficiently thick wells[30]. In Fig. 2(a), we present the energy levels at $k_\perp = 0$ for the lowest CB subband (E_0), the highest LH subband (L_0) and the highest HH subband (H_0) as a function of the barrier thickness, L_b. The inset shows the amplitude of the built-in electric field in wells ($|F_{qw}|$) versus L_b. Note that increasing L_b results in increase of $|F_{qw}|$, according to the well-known formula $F_{qw} = \frac{L_b(P_b - P_{qw})}{L_{qw}\lambda_b + L_b\lambda_{qw}}$, where P_{qw} and P_b denote the polarization in wells and barriers and λ is the electric permittivity[13–15]. As a consequence, the E_0 level decreases and the L_0 and H_0 levels increase with increasing L_b in accordance with the quantum confined Stark effect[13–15]. Due to the negative SOC in InN, the L_0 level is above the H_0 level. For L_b near 15 nm, we observe the anticrossing between the E_0 and L_0 levels, since both states transform according to the Γ_7 irreducible representations. In Fig. 2(b), we show the E_{2Dg} as a function of L_b. One can see that the E_{2Dg} closes first for $L_b = 15.06$ nm due to the TPT originating from the inversion of the CB and LH subbands. Then, the E_{2Dg} vanishes
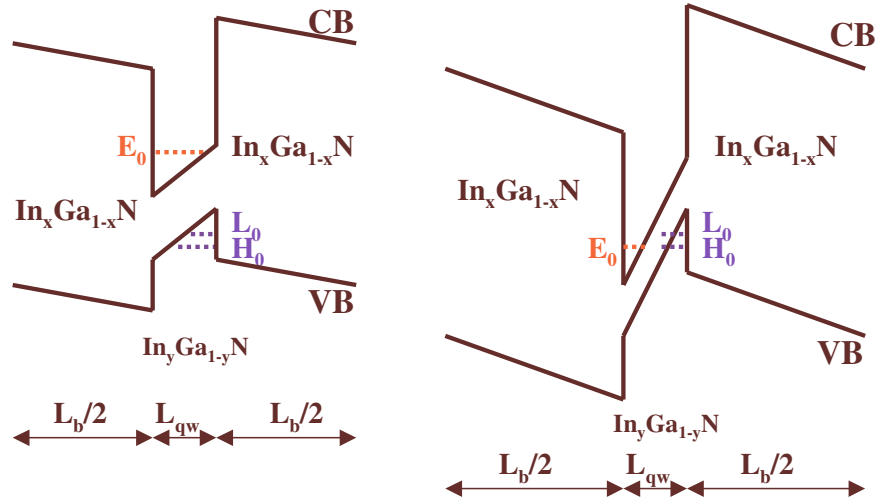
(a) Normal insulator   (b) Topological insulator

Figure 1. Schematic representation of InGaN-based QWs in the NI (**a**) and TI (**b**) phases. The thickness of $In_yGa_{1−y}N$ QWs is denoted by L_{qw} and L_b is the width of $In_xGa_{1−x}N$ barriers. The energy levels E_0, L_0 and H_0 correspond to the lowest CB level and the highest LH and HH levels, respectively.

for L_b larger than 21 nm due to the transition from the TI phase to the nonlocal semimetal (NSM) phase, arising from nonlocal overlapping between the LH and HH subbands[14]. The largest value of the E_{2Dg} in the TI state is about 1.25 meV, which is a few times smaller than it was predicted assuming the positive SOC in InN[13–15]. Nevertheless, the obtained values of the E_{2Dg} are still large enough to allow experimental verification of the edge state transport in InN/GaN QWs. Here, we would like to mention that the TI state with the E_{2Dg} of about 1–3 meV has recently been found experimentally in HgTe/CdHgTe QWs[31]. In order to confirm the TPT in InN/GaN QWs, we compute electronic states in a Hall bar represented by a strip structure with the width of 1000 nm. The Hall bar contains InN/GaN QWs with $L_{qw} = 1.25$ nm and $L_b = 16$ nm, which are in the TI state. Figure 2(c) shows the dispersion of electronic states obtained using the 2D effective Hamiltonian, which has been described in the Methods section. One can see metallic edge states arising from the quantum spin Hall effect in the 2D TIs[1]. Unlike the previous studies[13–15], we find that the Dirac point of the edge states dispersion curve is located near the middle of the E_{2Dg}, due to the anomalous ordering of the LH and HH subbands, originating from the negative SOC in InN. Now, we focus on the WSM phase occurring when the system goes through the TPT. In Fig. 2(d), we present the CB and LH subbands in InN/GaN QWs with $L_{qw} = 1.25$ nm and $L_b = 15.06$ nm. The obtained WSM can be described by the critical magnitude of the in-plane wave vector $k_0 = 0.0015$ Å$^{−1}$ and the anticrossing of the energy levels $\Delta_0 = E_0 − L_0$ equal to 1.1 meV.

We extend our study to InN/$In_xGa_{1−x}N$ QWs. We consider multi-QW structures pseudomorphically grown on unstrained $In_xGa_{1−x}N$ buffer layers, acting as virtual substrates. In these structures, the magnitude of internal strain decreases linearly with increasing the In content in barriers, which significantly facilitates pseudomorphic growth. It is worth mentioning that $In_xGa_{1−x}N$ layers can be grown over the entire composition range and they have already been used as virtual substrates in the growth of $In_yGa_{1−y}N$/$In_xGa_{1−x}N$ QWs for optoelectronic applications[32,33]. We focus on multi-QWs with wide barriers (similarly to refs[13–15], we take $L_b = 40$ nm), since in these structures, $|F_{qw}|$ is much larger than the amplitude of the built-in electric field in the barriers ($|F_b| = |F_{qw}|L_{qw}/L_b$) and the TPT can be more easily obtained[13–15]. Note that the dependence of $|F_{qw}|$ on L_b is rather weak for large L_b and thus, we study the TPT in InN/$In_xGa_{1−x}N$ QWs as a function of L_{qw} and In content in the barriers, for fixed L_b. In Fig. 3(a), we show a phase diagram illustrating four phases, i.e., the NI, the WSM, the TI, and the NSM, for InN/$In_xGa_{1−x}N$ QWs with L_{qw} in the range from 1.5 to 4 nm. Dotted line represents the critical In content in the barriers of InN/$In_xGa_{1−x}N$ heterostructures, x_c, above which pseudomorphic growth without strain relaxation is possible. The dependence of x_c on L_{qw} is obtained using a modification of the model of Fischer-Kühne-Richter[34]. For each value of L_{qw}, all four phases can be achieved in pseudomorphic InN/$In_xGa_{1−x}N$ QWs by properly choosing the composition of the barriers. Note, that the distance between the solid and dotted lines increases with increasing L_{qw}, which indicates that the band inversion can be obtained easier in wider QWs with larger In content in the barriers. However, the properties of the TI state deteriorate with increasing L_{qw}, as we demonstrate in Fig. 3(b). For each L_{qw}, the TI phase can be characterized by the window of In content within which the TI state is achieved, Δx_{TI}, and by the largest value of the E_{2Dg}, which is denoted by $E_{2Dg, max}$. In Fig. 3(b), we show the Δx_{TI} (left axis) and the $E_{2Dg, max}$ (right axis) as a function of L_{qw}. One can see that the Δx_{TI} decreases with increasing L_{qw} and the $E_{2Dg, max}$ reaches the largest value of 2 meV for relatively narrow QWs with $L_{qw} = 1.8$ nm. The TI state with the $E_{2Dg, max} = 2$ meV is found for 1.8 nm wide InN/$In_{0.316}Ga_{0.684}N$ QWs. In Fig. 3(c), we present the parameters k_0 (left axis) and Δ_0 (right axis) for the WSM in InN/$In_xGa_{1−x}N$ QWs as a function of L_{qw}. One can see that
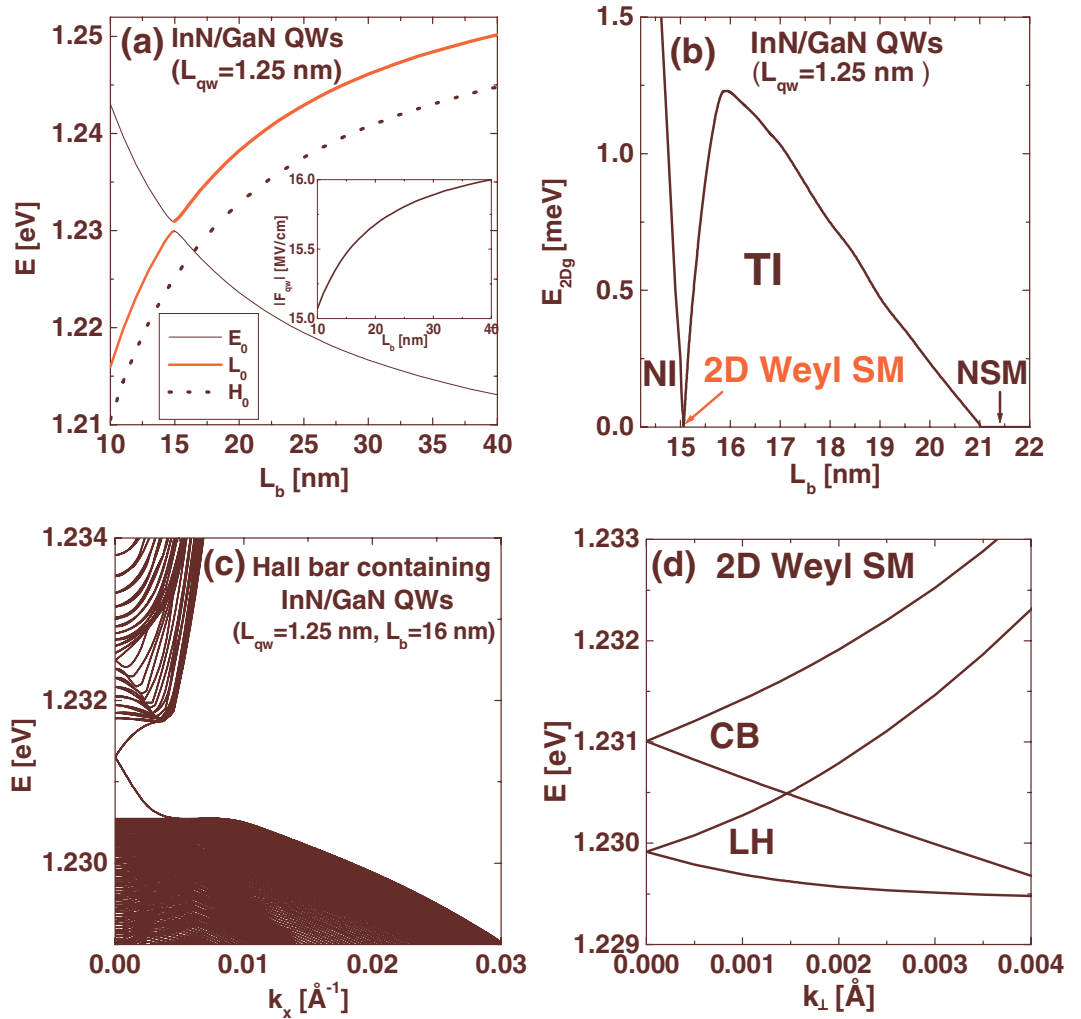
Figure 2. (**a,b**) The energy levels E_0, L_0, and H_0 (**a**), and the E_{2Dg} (**b**) in InN/GaN QWs with $L_{qw} = 1.25$ nm as a function of L_b. The inset in (**a**) shows the amplitude of the built-in electric field in wells versus L_b. (**c**) The dispersion of electronic states in a 1000 nm wide Hall bar structure containing InN/GaN QWs with $L_{qw} = 1.25$ nm and $L_b = 16$ nm. (**d**) The CB and LH subbands in the WSM phase for InN/GaN QWs with $L_{qw} = 1.25$ nm and $L_b = 15.06$ nm.

both k_0 and Δ_0 are significant and show no tendency to vanish simultaneously, which indicates that in InN/In$_x$Ga$_{1-x}$N QWs, we deal solely with the WSM between the NI and TI phases.

Finally, we consider In$_y$Ga$_{1-y}$N/GaN multi-QWs with wide barriers ($L_b = 40$ nm), which are grown on GaN substrate. Figure 4(a) shows the In content, for which the TPT occurs (dashed line) and the critical In content for pseudomorphic growth y_c, obtained using the Fischer-Kühne-Richter model (solid line)[34], as a function of L_{qw}. We find that the TPT can be achieved only in the QWs with L_{qw} smaller than 1.9 nm, for which pseudomorphic growth is possible. The dotted line separates the QWs, for which the highest LH subband is above the highest HH subband ($L_0 > H_0$), from those QWs having the opposite ordering of the valence subbands ($H_0 > L_0$). Above the dotted line, we have $L_0 > H_0$ and thus, in pseudomorphically grown In$_y$Ga$_{1-y}$N/GaN QWs, the TPT occurs always due to inversion of the highest LH subband and the lowest CB subband. In Fig. 4(b), we show the window of In content within which the TI state is achieved, Δy_{TI} (left axis), and the $E_{2Dg, \, max}$ (right axis) as a function of L_{qw}. Both these parameters decrease with increasing L_{qw}, which indicates that the properties of the TI state deteriorate for wider In$_y$Ga$_{1-y}$N/GaN QWs. The dotted lines in Figs 4(b,c) correspond to the QW structures, for which the In content is larger than y_c, and thus, non-pseudomorphic growth with partial strain relaxation can occur. Figure 4(c) presents the parameters k_0 (left axis) and Δ_0 (right axis) for the WSM occurring when the system goes through the TPT. Interestingly, both k_0 and Δ_0 vanish for $L_{qw} = 1.86$ nm, which indicates that in this particular case, the TPT is mediated by the DSM instead of the WSM. Indeed, as shown in Fig. 4(d), for In$_{0.838}$Ga$_{0.162}$N/GaN QWs with $L_{qw} = 1.86$ nm, we obtain a crossing of the E_0 and L_0 levels that leads to the appearance of the DSM. In order to find an explanation of this effect, we compute the average $\Delta_{so}^{\perp}$ parameter over a QW structure at the LH and CB states for $k_{\perp} = 0$. Note that $\Delta_{so}^{\perp}$ couples different spins in the valence band states and determines the coupling between the LH and CB states at $k_{\perp} = 0$ (see the Methods section). The results are presented in the inset in Fig. 4(c). One
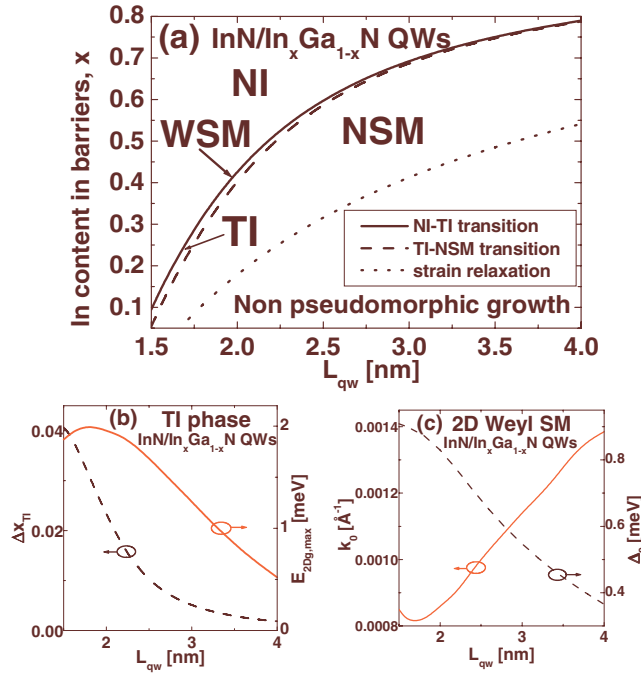
Figure 3. (**a**) The phase diagram illustrating four phases, i.e., the NI, the WSM, the TI, and the NSM, in InN/In$_x$Ga$_{1-x}$N QWs with $L_b = 40$ nm. Dotted line corresponds to the critical In content in the barriers, x_c, above which pseudomorphic growth is possible. (**b**) The Δx_{TI} (left axis) and the $E_{2Dg, \text{max}}$ (right axis) in InN/In$_x$Ga$_{1-x}$N QWs as a function of L_{qw}. (**c**) The parameters k_0 (left axis) and Δ_0 (right axis) for the WSM as a function of L_{qw}.

can see that the average $\Delta_{so}^\perp$ vanishes exactly for the same QW structure, for which the DSM appears. Vanishing of the average $\Delta_{so}^\perp$ is possible, since the $\Delta_{so}^\perp$ parameter has different signs in wells ($\Delta_{so}^\perp = -2.32$ meV) and barriers ($\Delta_{so}^\perp = 16.2$ meV). Importantly, the observed transition between the WSM and the DSM occurs without changing the crystal symmetry of QWs or the reordering of the valence subbands. This new phenomenon can be verified by several experimental methods including magnetotransport experiments and THz radiation absorption measurements, which have recently been proposed to study the gapless states in HgTe/CdTe QWs[9].

To conclude, we have demonstrated that in InN/In$_x$Ga$_{1-x}$N and In$_y$Ga$_{1-y}$N/GaN QWs, the negative SOC is not an obstacle to induce the TI state with the significant E_{2Dg}, enabling measurements of edge state transport in reasonable conditions. The magnitude of E_{2Dg} decreases with increasing L_{qw} in In$_y$Ga$_{1-y}$N/GaN QWs, whereas in InN/In$_x$Ga$_{1-x}$N QWs, it shows a non-monotonic dependence on L_{qw}, with the largest value of 2 meV reached for 1.8 nm wide InN/In$_{0.316}$Ga$_{0.684}$N QWs. The TPT in InGaN-based QWs is usually mediated by the WSM arising from the anticrossing of the CB and LH levels at $k_\perp = 0$. However, for certain In$_y$Ga$_{1-y}$N/GaN QWs, we have found that this anticrossing vanishes, leading to the appearance of the DSM. The novel transition between the WSM and the DSM occurs due to vanishing of the average $\Delta_{so}^\perp$ parameter in the QW system. This effect originates from opposite signs of the $\Delta_{so}^\perp$ parameter in wells and barriers without changing the system symmetry or the reordering of the valence subbands. Thus, our work reveals that InGaN-based QWs with inverted bands represent a unique topological QW system, which differs significantly from the conventional 2D TIs based on HgTe/CdTe and InAs/GaSb/AlSb QWs. We hope that these results will stimulate intensive theoretical and experimental studies towards fabrication and investigation of group-III nitride topological materials and devices. Since the negative SOC occurs also in HgS and TlN, the similar effects to these observed in InGaN-based QWs may appear in other 2D topological nanostructures.

Methods

In this section, we provide the details on the eight-band $\boldsymbol{k \cdot p}$ method, which we apply to calculate the subband dispersion in InGaN-based QWs. Our approach includes relativistic and nonrelativistic linear-$\boldsymbol{k}$ terms, which play a significant role in accurate determination of the valence bands of GaN and InN[26]. We also determine the effective 2D Hamiltonian, which is used to calculate the electronic states in a Hall bar containing InN/GaN QWs.

According to refs[26,35], the 6×6 valence band $\boldsymbol{k \cdot p}$ Hamiltonian for unstrained wurtzite semiconductors can be written as

$$
\begin{aligned}
H^{6 \times 6} = {} & \Delta_1 J_z^2 + \Delta_2 J_z \sigma_z + \sqrt{2}\,\Delta_3 (J_+ \sigma_- + J_- \sigma_+) + (A_1 + A_3 J_z^2)k_z^2 + (A_2 + A_4 J_z^2)k_\perp^2 - A_5(J_+^2 k_-^2 + J_-^2 k_+^2) \\
& - 2iA_6 k_z(\{J_z, J_+\}k_- - \{J_z, J_-\}k_+) + A_7(k_- J_+ + k_+ J_-) + (\alpha_1 + \alpha_3 J_z^2)(\sigma_+ k_- + \sigma_- k_+) \\
& + \alpha_2(J_+^2 \sigma_- k_- + J_-^2 \sigma_+ k_+) + 2\alpha_4 \sigma_z(\{J_z, J_+\}k_- - \{J_z, J_-\}k_+) + 2i\alpha_5 k_z(\{J_z, J_+\}\sigma_- - \{J_z, J_-\}\sigma_+)
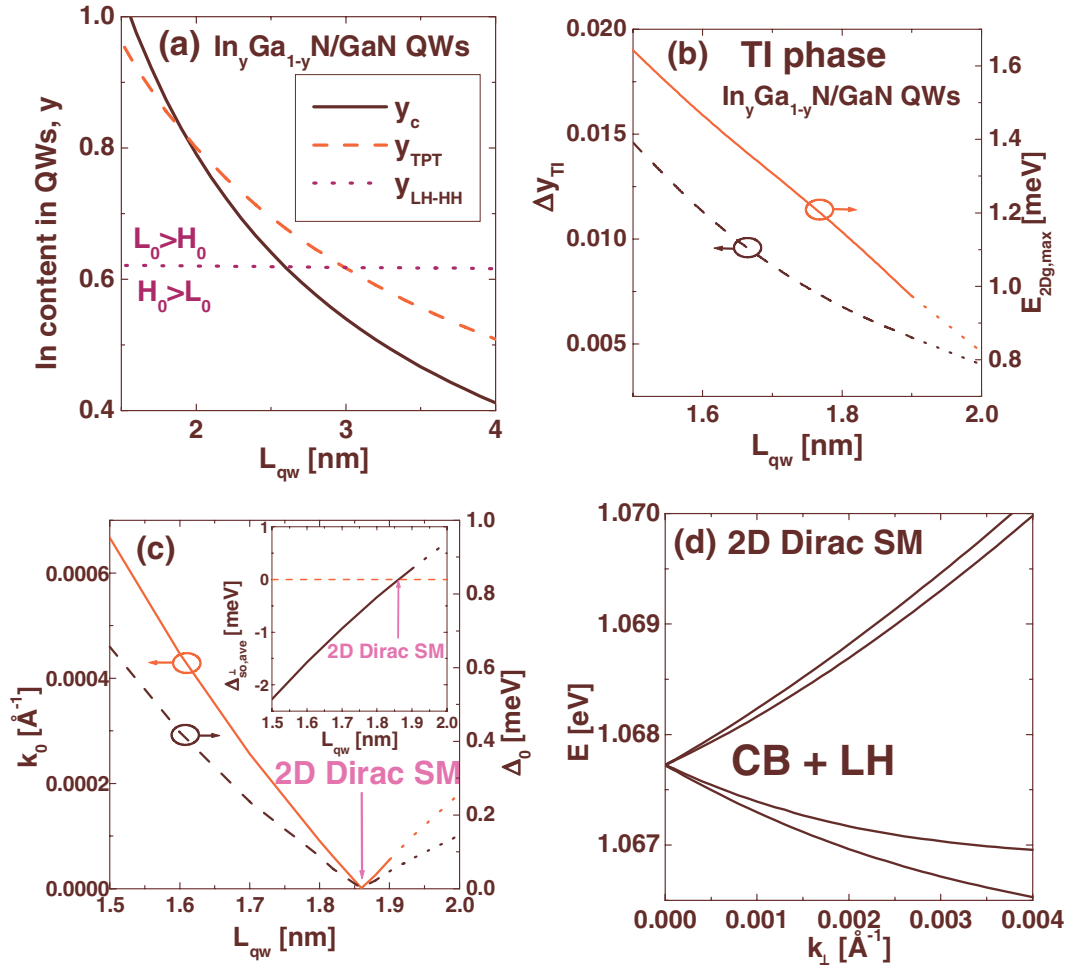\end{aligned}
\tag{1}
$$

Figure 4. (**a**) In content in $In_yGa_{1-y}N$/GaN QWs, for which the TPT occurs (dashed line) and the critical In content for pseudomorphic growth, y_c (solid line), as a function of L_{qw}. Above the dotted line, the highest LH subband has higher energy than the highest HH subband. (**b**) The values of Δy_{TI} (left axis) and $E_{2Dg,\ max}$ (right axis) for the TI phase in $In_yGa_{1-y}N$/GaN QWs as a function of L_{qw}. (**c**) The parameters k_0 (left axis) and Δ_0 (right axis) for the WSM as a function of L_{qw}. The inset shows the average $\Delta_{so}^{\perp}$ parameter over a QW structure at the E_0 and L_0 states as a function of L_{qw}. The dotted lines in (**b**) and (**c**) represent the QW structures, for which the In content is larger than y_c. (**d**) The CB and LH subbands in the DSM state for $In_{0.838}Ga_{0.162}N$/GaN QWs with $L_{qw} = 1.86$ nm and $L_b = 40$ nm.

where $J_{\pm} = \frac{1}{\sqrt{2}}(\pm iJ_x - J_y)$, $\sigma_{\pm} = \frac{1}{\sqrt{2}}(\pm i\sigma_x - \sigma_y)$, $\{J_z, J_+\} = \frac{1}{2}(J_zJ_+ + J_+J_z)$, $k_{\pm} = k_x \pm ik_y$, $k_{\perp}^2 = k_x^2 + k_y^2$. The parameters $\Delta_1, \Delta_2 = \Delta_{so}^{\parallel}/3$, and $\Delta_3 = \Delta_{so}^{\perp}/3$ are the crystal field splitting and the spin-orbit coupling splittings, respectively. The parameters $A_1, ..., A_6$ are inverse effective-mass type parameters, the A_7 coefficient determines a nonrelativistic linear-$\boldsymbol{k}$ term and the parameters $\alpha_1, ..., \alpha_5$ describe the relativistic (spin-dependent) terms linear in $\boldsymbol{k}$. The σ_x, σ_y, and σ_z denote the Pauli spin matrices and the J_x, J_y, and J_z are the angular momentum matrices:

$$J_x = \frac{1}{\sqrt{2}}\begin{bmatrix} 0 & 1 & 0 \\ 1 & 0 & 1 \\ 0 & 1 & 0 \end{bmatrix}, \quad J_y = \frac{i}{\sqrt{2}}\begin{bmatrix} 0 & -1 & 0 \\ 1 & 0 & -1 \\ 0 & 1 & 0 \end{bmatrix}, \quad J_z = \begin{bmatrix} 1 & 0 & 0 \\ 0 & 0 & 0 \\ 0 & 0 & -1 \end{bmatrix}.$$

The Hamiltonian $H^{6\times6}$ can be represented in a matrix form as follows:

$$H^{6\times6} = \begin{bmatrix} F & K^* & M^* & 0 & -W^* & 0 \\ K & G & -N_+ & -W^* & -T & \Delta \\ M_- & -N_+^* & L & 0 & \Delta^* & -S^* \\ 0 & -W & 0 & F & K & -M_+ \\ -W & -T^* & \Delta & K^* & G & N_-^* \\ 0 & \Delta^* & -S & -M_+^* & N_- & L \end{bmatrix} \begin{matrix} |-(X+iY)/\sqrt{2},\uparrow\rangle \\ |(X-iY)/\sqrt{2},\uparrow\rangle \\ |Z,\uparrow\rangle \\ |(X-iY)/\sqrt{2},\downarrow\rangle \\ |-(X+iY)/\sqrt{2},\downarrow\rangle \\ |Z,\downarrow\rangle \end{matrix} , \qquad (2)$$

where $F = \Delta_1 + \Delta_2 + (A_2 + A_4)k_\perp^2 + (A_1 + A_3)k_z^2$, $G = F - 2\Delta_2$, $L = A_2 k_\perp^2 + A_1 k_z^2$, $K = A_5 k_+^2$, $M_+ = [A_6 k_z + i(A_7 + \alpha_4)]k_+$, $M_- = [A_6 k_z - i(A_7 + \alpha_4)]k_+$, $N_+ = [A_6 k_z + i(A_7 - \alpha_4)]k_+$, $N_- = [A_6 k_z - i(A_7 - \alpha_4)]k_+$, $\Delta = \sqrt{2}\Delta_3 + i\alpha_5 k_z$, $S = i\alpha_1 k_+$, $T = i\alpha_2 k_+$, and $W = i(\alpha_1 + \alpha_3)k_+$.

The above Hamiltonian can be reduced to the **k·p** Hamiltonians presented in refs[36,37] by neglecting the relativistic and nonrelativistic linear-**k** terms. Here, we note that the coefficients A_5 and A_6 have opposite signs to those in refs[36,37]. (The difference in sign of the A_5 and A_6 coefficients was also discussed in refs[38,39]) In order to take into account the coupling between the conduction band and the valence bands, we enlarge the Hamiltonian (2) to the eight-band model using the approach applied in refs[13,14]. We reduce the parameter Δ to $\sqrt{2}\Delta_3$, since $\alpha_5 = 0$ for GaN and InN[26]. The resulting $H^{8\times8}$ Hamiltonian has the form

$$H^{8\times8} = \begin{bmatrix} H_c & -Q & Q^* & R & 0 & 0 & 0 & 0 \\ -Q^* & F & K^* & M_-^* & 0 & 0 & -W^* & 0 \\ Q & K & G & -N_+ & 0 & -W^* & -T & \sqrt{2}\Delta_3 \\ R & M_- & -N_+^* & L & 0 & 0 & \sqrt{2}\Delta_3 & -S^* \\ 0 & 0 & 0 & 0 & H_c & Q^* & -Q & R \\ 0 & 0 & -W & 0 & Q & F & K & -M_+ \\ 0 & -W & -T^* & \sqrt{2}\Delta_3 & -Q^* & K^* & G & N_-^* \\ 0 & 0 & \sqrt{2}\Delta_3 & -S & R & -M_+^* & N_- & L \end{bmatrix} \begin{matrix} |iS, \uparrow\rangle \\ |-(X+iY)/\sqrt{2}, \uparrow\rangle \\ |(X-iY)/\sqrt{2}, \uparrow\rangle \\ |Z, \uparrow\rangle \\ |iS, \downarrow\rangle \\ |(X-iY)/\sqrt{2}, \downarrow\rangle \\ |-(X+iY)/\sqrt{2}, \downarrow\rangle \\ |Z, \downarrow\rangle \end{matrix} \tag{3}$$

where $H_c = E_{vb} + E_g + A_{c\perp}k_\perp^2 + A_{c||}k_z^2$, $Q = P_2 k_+/\sqrt{2}$, and $R = P_1 k_z$. The top valence band energy and the energy gap are denoted by E_{vb} and E_g, respectively, $A_{c\perp}$ and $A_{c||}$ describe the dispersion of the conduction band, whereas P_1 and P_2 are the Kane parameters[37]. The parameters $A_1, ..., A_6$ occurring in the valence band part of the Hamiltonian $H^{8\times8}$ have to be rescaled according to ref[40].

In order to determine the electronic states in a QW grown along [0001] crystallographic direction of the wurtzite structure, we include the strain effects and the built-in electric field originating from the piezoelectric effect and the spontaneous polarization[14,15]. Due to large lattice misfit between GaN and InN, we calculate strain and the built-in electric field taking into account the effects of nonlinear elasticity and nonlinear piezoelectricity, according to refs[14,15,41]. Then, replacing k_z in the Hamiltonian $H^{8\times8}$ by the operator $-i\frac{\partial}{\partial z}$, we get the eight-band Schrödinger-type equation,

$$\sum_{\beta=1}^{8} H_{\alpha,\beta}^{8\times8}\left(\overrightarrow{k_\perp}, k_z = -i\frac{\partial}{\partial z}\right)F_{m,\beta}(z, \overrightarrow{k_\perp}) = E_m(\overrightarrow{k_\perp})F_{m,\alpha}(z, \overrightarrow{k_\perp}), \quad \alpha = 1, ..., 8, \tag{4}$$

where $E_m(\overrightarrow{k_\perp})$ and $F_{m,\beta}(z, \overrightarrow{k_\perp})$ are the energies and the envelope functions of the QW states. Since in QW heterostructures, the material parameters depend on position, we use the standard symmetrization to ensure the Hermiticity of operators containing the product of functions and derivatives[14]. The subband dispersion in InN/GaN, InN/InGaN, and InGaN/GaN QWs is obtained by solving numerically Eq. (4)[14].

To calculate the electronic states in a Hall bar structure of finite width, represented by infinitely long strip in the QW plane, we focus on the lowest CB subband and the highest LH and HH subbands. For these subbands, we generate the 6×6 effective 2D Hamiltonian, using the mini-band **k·p** method and the Löwdin perturbation approach[13,14]. In the first step, we define the z-direction averaged Hamiltonian

$$H_{m,n} = \left\langle \Psi_{m,\overrightarrow{k_\perp}}|H^{8\times8}\left(\overrightarrow{k_\perp}, k_z = -i\frac{\partial}{\partial z}\right)|\Psi_{n,\overrightarrow{k_\perp}}\right\rangle = \sum_{\alpha,\beta=1}^{8}\int dz F_{m,\alpha}^*(z)H_{\alpha,\beta}^{8\times8}F_{n,\beta}(z), \tag{5}$$

where $\Psi_{m,\overrightarrow{k_\perp}} = e^{i\overrightarrow{k_\perp}\overrightarrow{r_\perp}}[F_{m,1}(z), ..., F_{m,8}(z)]^T$ is the Luttinger-Kohn basis set for the mini-band **k·p** method in the vicinity of the Γ point, and $F_{m,\alpha}(z) = F_{m,\alpha}(z, \overrightarrow{k_\perp} = 0)$. This Hamiltonian can be divided into two parts $H_{m,n} = H_{m,n}^0 + H_{m,n}'$, where

$$H_{m,n}^0 = \left\langle \Psi_{m,\overrightarrow{k_\perp}}|H^{8\times8}\left(\overrightarrow{k_\perp} = 0, k_z = -i\frac{\partial}{\partial z}\right)|\Psi_{n,\overrightarrow{k_\perp}}\right\rangle = \delta_{m,n}E_m(\overrightarrow{k_\perp} = 0), \tag{6}$$

and

$$H_{m,n}' = \left\langle \Psi_{m,\overrightarrow{k_\perp}}|H'^{8\times8}\left(\overrightarrow{k_\perp}, k_z = -i\frac{\partial}{\partial z}\right)|\Psi_{n,\overrightarrow{k_\perp}}\right\rangle = \sum_{\alpha,\beta=1}^{8}\int dz F_{m,\alpha}^*(z)H_{\alpha,\beta}'^{8\times8}F_{n,\beta}(z). \tag{7}$$

Then, we consider six eigenstates of the Hamiltonian $H_{m,n}^0$: $|E, j_z = \pm 1/2\rangle$, $|LH, j_z = \pm 1/2\rangle$, and $|HH, j_z = \pm 3/2\rangle$, corresponding to the lowest CB subband and the highest LH and HH subbands, respectively. The symbol j_z denotes the projection of the total angular momentum on the z-axis. The coupling between the six states $|E, j_z = \pm 1/2\rangle$, $|LH, j_z = \pm 1/2\rangle$, $|HH, j_z = \pm 3/2\rangle$ and the rest of the eigenstates of the Hamiltonian $H_{m,n}^0$ can be eliminated to the second order in **k** using the Löwdin perturbation method[13,14]. For practical implementation, we consider additional 114 states of the Hamiltonian $H_{m,n}^0$ corresponding to 19 double degenerated levels for the CB, LH and HH subbands. The effective Hamiltonian has the following form:
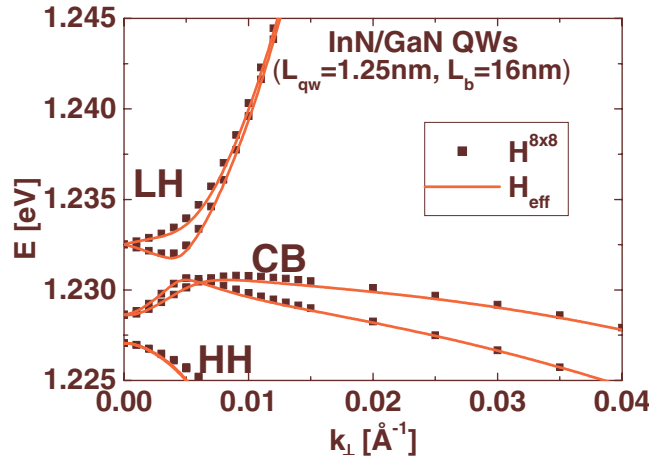
Figure 5. The subband dispersion in InN/GaN QWs with $L_{qw} = 1.25$ nm and $L_b = 16$ nm, obtained using the eight-band **k·p** Hamiltonian, $H^{8\times8}$, (squares) and the effective 2D Hamiltonian, H_{eff} (solid lines).

$$H_{eff} = \begin{bmatrix} E_0 + E_1 k_\perp^2 & C_2 k_- & C_1 k_+ & iC_3 k_- & iMk_\perp^2 & iB_2 k_-^2 \\ C_2 k_+ & L_0 + L_1 k_\perp^2 & B_1 k_+^2 & -iMk_\perp^2 & iC_4 k_+ & iC_5 k_- \\ C_1 k_- & B_1 k_-^2 & H_0 + H_1 k_\perp^2 & -iB_2 k_-^2 & iC_5 k_- & 0 \\ -iC_3 k_+ & iMk_\perp^2 & iB_2 k_+^2 & E_0 + E_1 k_\perp^2 & -C_2 k_+ & -C_1 k_- \\ -iMk_\perp^2 & -iC_4 k_- & -iC_5 k_+ & -C_2 k_- & L_0 + L_1 k_\perp^2 & B_1 k_-^2 \\ -iB_2 k_+^2 & -iC_5 k_+ & 0 & -C_1 k_+ & B_1 k_+^2 & H_0 + H_1 k_\perp^2 \end{bmatrix} \begin{matrix} |E, 1/2\rangle \\ |LH, -1/2\rangle \\ |HH, 3/2\rangle \\ |E, -1/2\rangle \\ |LH, 1/2\rangle \\ |HH, -3/2\rangle \end{matrix} \qquad (8)$$

where E_0, L_0, and H_0 correspond to the energies of states $|E, j_z = \pm 1/2\rangle$, $|LH, j_z = \pm 1/2\rangle$, and $|HH, j_z = \pm 3/2\rangle$, respectively. The obtained Hamiltonian H_{eff} has the same form to that used in refs[14,15]. The linear-**k** terms of the Hamiltonian $H^{8\times8}$ with the coefficients $\alpha_1, ..., \alpha_4$ and A_7 do not change the structure of H_{eff}, but they contribute significantly to the values of the coefficients $C_1, ..., C_5$.

In Fig. 5, we compare the subband dispersions for an exemplary InN/GaN multi-QW structure ($L_{qw} = 1.25$ nm and $L_b = 16$ nm) obtained using the $H^{8\times8}$ Hamiltonian (squares) and the Hamiltonian H_{eff} (solid lines). We find that the Hamiltonian H_{eff} describes quite well the in-plane dispersion of the lowest CB subband and the highest LH and HH subbands and thus, it can be applied to calculate the electronic states in a Hall bar.

In the calculations of the electronic states in InN/GaN QWs, we use the valence band parameters from ref[26] and the deformation potentials from ref[13]. For InN/InGaN and InGaN/GaN QWs, we apply the valence band parameters from ref[26] (assuming linear dependence on composition in InGaN), the deformation potentials from ref[42]. We determine the spontaneous polarization and the piezoelectric polarization according to ref[41]. Nonlinear dependence on composition in InGaN is taken into account for the first-order piezoelectric constants, whereas in the case of the spontaneous polarization and the second-order piezoelectric constants, linear dependence on composition is assumed[41]. The second-order elastic constants and the third-order elastic constants (assuming linear dependence on composition in InGaN) are taken from ref[43] and ref[14], respectively.

Data Availability

The datasets generated and analysed during the current study are available from the corresponding author on reasonable request.

References

1. Hasan, M. Z. & Kane, C. L. Colloquium: Topological insulators. *Rev. Mod. Phys.* **82**, 3045 (2010).
2. Murakami, S. & Kuga, S.-I. Universal phase diagrams for the quantum spin Hall systems. *Phys. Rev. B* **78**, 165313 (2008).
3. Murakami, S., Hirayama, M., Okugawa, R. & Miyake, T. Emergence of topological semimetals in gap closing in semiconductors without inversion symmetry. *Sci. Adv.* **3**, e1602680 (2017).
4. Young, S. M. *et al.* A. M. Dirac semimetal in three dimensions. *Phys. Rev. Lett.* **108**, 140405 (2012).
5. Armitage, N. P., Mele, E. J. & Vishwanath, A. Weyl and Dirac semimetals in three-dimensional solids. *Rev. Mod. Phys.* **90**, 015001 (2018).
6. Juricic, V., Abergel, D. S. L. & Balatsky, A. V. First-order quantum phase transition in three-dimensional topological band insulators. *Phys. Rev. B* **95**, 161403(R) (2017).
7. Murakami, S., Iso, S., Avishai, Y., Onoda, M. & Nagaosa, N. Tuning phase transition between quantum spin Hall and ordinary insulating phases. *Phys. Rev. B* **76**, 205304 (2007).
8. Winkler, R., Wang, L. Y., Lin, Y. H. & Chu, C. S. Robust level coincidences in the subband structure of quasi-2D systems. *Solid State Commun.* **152**, 2096 (2012).
9. Tarasenko, S. A. *et al.* Split Dirac cones in HgTe/CdTe quantum wells due to symmetry-enforced level anticrossing at interfaces. *Phys. Rev. B* **91**, 081302(R) (2015).

10. Klipstein, P. C. Structure of the quantum spin Hall states in HgTe/CdTe and InAs/GaSb/AlSb quantum wells. *Phys. Rev. B* **91**, 035310 (2015).
11. Ahn, J. & Yang, B.-J. Unconventional topological phase transition in two-dimensional systems with space-time inversion symmetry. *Phys. Rev. Lett.* **118**, 156401 (2017).
12. Young, S. M. & Kane, C. L. Dirac semimetals in two dimensions. *Phys. Rev. Lett.* **115**, 126803 (2015).
13. Miao, M. *et al.* Polarization-driven topological insulator transition in a GaN/InN/GaN quantum well. *Phys Rev. Lett.* **109**, 186803 (2012).
14. Łepkowski, S. P. & Bardyszewski, W. Topological phase transition and evolution of edge states in In-rich InGaN/GaN quantum wells under hydrostatic pressure. *J. Phys.: Condens. Matter* **29**, 055702 (2017).
15. Łepkowski, S. P. & Bardyszewski, W. Anomalous Rashba spin-orbit interaction in electrically controlled topological insulator based on InN/GaN quantum wells. *J. Phys.: Condens. Matter* **29**, 195702 (2017).
16. Gorczyca, I., Suski, T., Strak, P., Staszczak, G. & Christensen, N. E. Band gap engineering of In(Ga)N/GaN short period superlattices. *Sci. Rep.* **7**, 16055 (2017).
17. Li., J & Chang, K. Electric field driven quantum phase transition between band insulator and topological insulator. *Appl. Phys. Lett.* **95**, 222110 (2009).
18. Liu, C., Hughes, T. L., Qi, X.-L., Wang, K. & Zhang, S.-C. Quantum spin Hall effect in inverted type-II semiconductors. *Phys Rev. Lett.* **100**, 236601 (2008).
19. Zhang, D., Lou, W., Miao, M., Zhang, S.-C. & Chang, K. Interface-induced topological insulator transition in GaAs/Ge/GaAs quantum wells. *Phys Rev. Lett.* **111**, 156402 (2013).
20. Liu, Q., Zhang, X., Abdalla, L. B. & Zunger, A. Transforming common III-V and II-VI semiconductor compounds into topological heterostructures: the case of CdTe/InSb superlattices. *Adv. Funct. Mater.* **26**, 3259 (2016).
21. Vurgaftman, I. & Meyer, J. R. Band parameters for nitrogen-containing semiconductors. *J. Appl. Phys.* **94**, 3675 (2003).
22. de Carvalho, L. C., Schleife, A. & Bechstedt, F. Influence of exchange and correlation on structural and electronic properties of AlN, GaN, and InN polytypes. *Phys. Rev. B* **84**, 195105 (2011).
23. Lin, K. I., Chen, Y. J., Cheng, Y. C. & Gwo, S. Investigation of valence-band splitting in InN by low-temperature photoreflectance spectroscopy. *Jpn. J. Appl. Phys.* **54**, 031001 (2015).
24. Bardyszewski, W., Rodak, D. & Łepkowski, S. P. Magnetoconductance in InN/GaN quantum wells in topological insulator phase. *EPL* **118**, 27001 (2017).
25. Hu., G., Zhang, Y., Li, L. & Wang, Z. L. Piezotronic transistor based on topological insulators. *ASC Nano* **12**, 779 (2017).
26. Punya, A. & Lambrecht, W. R. L. Valence band effective-mass Hamiltonians for the group-III nitrides from quasiparticle self-consistent GW band structures. *Phys. Rev. B* **85**, 195147 (2012).
27. Svane, A. *et al.* Quasiparticle band structures of β-HgS, HgSe, and HgTe. *Phys. Rev. B* **84**, 205205 (2011).
28. Lambrecht, W. R. L., Rodina, A. V., Limpijumnong, S., Segall, B. & Meyer, B. K. Valence-band ordering and magneto-optic exciton fine structure in ZnO. *Phys. Rev. B* **65**, 075207 (2002).
29. Sheng, X.-L. *et al.* Topological insulator to Dirac semimetal transition driven by sign change of spin-orbit coupling in thallium nitride. *Phys. Rev. B* **90**, 245308 (2014).
30. Dimitrakopulos, G. P. *et al.* Compositional and strain analysis of In(Ga)N/GaN short period superlattices. *J. Appl. Phys.* **123**, 024304 (2018).
31. Olshanetsky, E. B. *et al.* Persistence of a two-dimensional topological insulator state in wide HgTe quantum wells. *Phys. Rev. Lett.* **114**, 126802 (2015).
32. Fabien, C. A. M. *et al.* Low-temperature growth of InGaN films over the entire composition range by MBE. *J. Cryst. Growth* **425**, 115 (2015).
33. Daubler, J. *et al.* Long wavelength emitting GaInN quantum wells on metamorphic GaInN buffer layers with enlarged in-plane lattice parameter. *Appl. Phys. Lett.* **105**, 111111 (2014).
34. Fischer, A., Kühne, H. & Richter, H. New approach in equilibrium theory for strained layer relaxation. *Phys. Rev. Lett.* **73**, 2712 (1994).
35. Bir, G. L. & Pikus, G. E. *Symmetry and Strain-Induced Effects in Semiconductors* (Wiley, New York, 1974).
36. Dugdale, D. J., Brand, S. & Abram, R. A. Direct calculation of **k·p** parameters for wurtzite AlN, GaN, and InN. *Phys. Rev. B* **61**, 12933 (2000).
37. Chuang, S. L. & Chang, C. S. **k·p** method for strained wurtzite semiconductors. *Phys. Rev. B* **54**, 2491 (1996).
38. Kim, K., Lambrecht, W. R. L., Segall, B. & van Schilfgaarde, M. Effective masses and valence-band splittings in GaN and AlN. *Phys. Rev. B* **56**, 7363 (1997).
39. Lew Yan Voon, L. C. & Willatzen, M. *The k·p Method* (Springer, Berlin Heidelberg, 2009).
40. Andreev, A. D. & O'Reilly, E. P. Theory of the electronic structure of GaN/AlN hexagonal quantum dots. *Phys. Rev. B* **62**, 15851 (2000).
41. Prodhomme, P.-Y., Beya-Wakata, A. & Bester, G. Nonlinear piezoelectricity in wurtzite semiconductors. *Phys. Rev. B* **88**, 121304 (2013).
42. Łepkowski, S. P., Gorczyca, I., Stefańska-Skrobas, K., Christensen, N. E. & Svane, A. Deformation potentials in AlGaN and InGaN alloys and their impact on optical polarization properties of nitride quantum wells. *Phys. Rev. B* **88**, 081202 (2013).
43. Łepkowski, S. P. Inapplicability of Martin transformation to elastic constants of zinc-blende and wurtzite group-III nitride alloys. *J. Appl. Phys.* **117**, 105703 (2015).

Author Contributions

Additional Information